

Title: Variation of Jupiter's Aurora Observed by Hisaki/EXCEED: 2. Estimations of Auroral Parameters and Magnetospheric Dynamics

Paper: JGR space physics

Authors: Chihiro Tao [1], Tomoki Kimura [2, 3], Sarah V. Badman [4], Nicolas André [1], Fuminori Tsuchiya [5], Go Murakami [2], Kazuo Yoshioka [2, 6], Ichiro Yoshikawa [7], Atsushi Yamazaki [2], Masaki Fujimoto [2]

Affiliations:

[1] IRAP, Université de Toulouse/UPS-OMP/CNRS, 9 avenue du Colonel Roche, 31028, Toulouse, France (chihiro.tao@irap.omp.eu)

[2] ISAS/JAXA, Sagamihara, Japan

[3] now at Riken, Saitama, Japan

[4] Lancaster University, Lancaster, UK

[5] Tohoku University, Miyagi, Japan

[6] now at Rikkyo University, Tokyo, Japan

[7] University of Tokyo, Tokyo, Japan

Corresponding Author: Chihiro Tao

Running title (≤ 40 characters): Jupiter's auroral parameters from Hisaki (40)

(~ 8200)/ $500 + 10 = 17 + 10 = 27$

Key points (≤ 80 characters):

1. Auroral electron energy and flux are estimated from Hisaki/EXCEED observations (78)
2. Aurora power enhancements are mainly due to increased electron flux, not energy (79)
3. Possible explanations for variations of estimated parameters are discussed (74)

This article has been accepted for publication and undergone full peer review but has not been through the copyediting, typesetting, pagination and proofreading process which may lead to differences between this version and the Version of Record. Please cite this article as doi: 10.1002/2015JA021272

Abstracts (<250 words)

[1] Jupiter's auroral parameters are estimated from observations by a spectrometer EXCEED (Extreme Ultraviolet Spectroscopy for Exospheric Dynamics) onboard JAXA's Earth-orbiting planetary space telescope Hisaki. EXCEED provides continuous auroral spectra covering the wavelength range over 80–148 nm from the whole northern polar region. The auroral electron energy is estimated using a hydrocarbon color ratio adopted for the wavelength range of EXCEED, and the emission power in the long wavelength range 138.5–144.8 nm is used as an indicator of total emitted power before hydrocarbon absorption and auroral electron energy flux. The quasi-continuous observations by Hisaki provide the auroral electron parameters and their relation under different auroral activity levels. Short- (within < one planetary rotation) and long-term (> one planetary rotation) enhancements of auroral power accompany increases of the electron number flux rather than the electron energy variations. The relationships between the auroral electron energy (~70–400 keV) and flux (10^{26} – 10^{27} /s, 0.08–0.9 $\mu\text{A}/\text{m}^2$) estimated from the observations over a 40-day interval are in agreement with field-aligned acceleration theory when incorporating probable magnetospheric parameters. Applying the electron acceleration theory to each observation point, we explore the magnetospheric source plasma variation during these power-enhanced events. Possible scenarios to explain the derived variations are (i) an adiabatic variation of the magnetospheric plasma under a magnetospheric compression and/or plasma injection, and (ii) a change of the dominant auroral component from the main emission (main aurora) to the emission at the open-closed boundary. (238 words)

1. Introduction

[2] Various magnetospheric regions may be mapped via the magnetic field onto a planetary upper atmosphere—specifically, to atmospheric regions which harbor auroral emissions. The spatial distribution and principal features of Jupiter's aurorae consists of the moon foot-print emissions, low-latitude emissions, the main auroral emission (main oval), and high latitude polar emissions, as we moved from the low to high latitudes [e.g., Grodent, 2014]. The main auroral emission is related with the plasma corotation-enforcement current responsible for transport of angular momentum from the planetary neutral atmosphere through the ionosphere to the magnetospheric plasma. Auroral emissions from Jupiter's polar region, enclosed by the main aurora, are suggested to reflect magnetospheric reconnection events and associated plasma flows [e.g., Grodent et al., 2004], emissions at the open-closed boundary and cusp [Pallier and Prangé, 2004], and short term bursts at the dayside cusp [e.g., Waite et al., 2001].

[3] Jupiter's aurorae are detected in various wavelengths which are sensitive to different processes [e.g., Badman et al., 2014]. Ultraviolet (UV) emissions are from atmospheric H₂ and H excited by precipitating auroral electrons. The far-UV (FUV) color ratio (CR), defined as the ratio of the intensity of a waveband unabsorbed by hydrocarbons to that of an absorbed one, is usually used to estimate the auroral electron energy from Jupiter's auroral emission [e.g., Gérard et al., 2003; 2014]. Since the precipitating electrons of higher energy can reach lower altitudes, the CR increases with electron energy. Applying this method to the observed Jovian aurorae, Gustin et al. [2004] revealed a positive correlation between the mean electron energy (30–200 keV) and the electron flux density ($\sim 0.04\text{--}0.4 \mu\text{A m}^{-2}$) of a Maxwellian distribution in

the form of a square root law, and they explained this dependence using Knight's acceleration theory [Knight, 1973]. Their fitting of the Knight relation suggests the obtained profiles are well within the magnetospheric parameter ranges observed by Voyager, i.e., a source electron temperature of ~ 2.5 keV with density of $0.001\text{--}0.01$ cm^{-3} . The high latitude auroral emission has two components: one has properties close to those of the main aurora ($\sim 0.05\text{--}0.2$ $\mu\text{A m}^{-2}$) and the other reflects electrons with smaller flux ($\sim 0.01\text{--}0.03$ $\mu\text{A m}^{-2}$) in the similar mean energy range of $30\text{--}200$ keV. A recent auroral model including energetic electrons proposes an updated energy-CR relation to find that energetic electrons precipitate into not only the polar region but also non-uniformly along the main auroral region [Gérard et al., 2014]. Auroral acceleration theories have also been adapted specifically to the jovian environment. One of these is a theoretical estimation by Cowley [2006] including relativistic effects which would be adequate for the very energetic (~ 100 keV) electrons sometimes detected at Jupiter, and which is compared by Gustin et al. [2006] with the bright auroral structure called dawn storms occasionally observed in the dawnside main oval. The current-voltage relation estimated from a Vlasov model applied to Jupiter indicates that the field-aligned currents are limited due to plasma confinement by the centrifugal force and the onset of a resulting ambipolar potential drop, which causes deviation from the Knight relation [e.g., Ray et al., 2009]. The Knight relation is well approximated by a linear explanation when the parallel potential drop Φ_{\parallel} is much larger than source electron energy $k_{\text{B}}T_0$, and the ratio between these two quantities remains small compared to the mirror ratio R_{M} , i.e., $1 \ll e\Phi_{\parallel} / k_{\text{B}}T_0 \ll R_{\text{M}}$, where e is elementary charge.

[4] The relation between current (electron flux) and voltage (electron energy) has been tested in other planetary environments as well. Those parameters estimated from Saturn's aurora are also consistent with the Knight relation based on the observed plasma parameters at Saturn's magnetospheric equator [Tao et al., 2014]. Various observation methods at Earth have shown both agreement and disagreement with the Knight relation [Morooka et al., 2004, and references therein]: the parallel conductance and field-aligned current measured at and above the field-aligned acceleration region are larger than those expected from the Knight relation due to the contribution of low energy electrons [Sakanoi et al., 1995; Morooka et al., 2004], while the current density determined by observations below the acceleration region is consistent with the Knight relation [e.g., Shiokawa et al., 1990].

[5] The spectrometer EXCEED (Extreme Ultraviolet Spectroscope for Exospheric Dynamics) [Yoshioka et al., 2013; Yoshikawa et al., 2014; Yamazaki et al., 2014] onboard JAXA's Earth-orbiting planetary telescope Hisaki monitors extreme UV (EUV) emissions from the Jovian aurora and Io plasma torus. Quasi-continuous observations over 40 min of every 106 min Hisaki orbit were conducted from December 2013 to April 2014. In addition, Hubble Space Telescope (HST) observations were also carried out during the first half of January 2014. Hisaki/EXCEED succeeded to detect sporadic, large (up to a factor of three) auroral power enhancements lasting less than 1 planetary rotation, as well as longer-term variations. The former are associated with auroral low latitude intensifications detected in the HST images [Kimura et al., 2015]. The latter are mostly accompanied by solar wind dynamic pressure enhancements. These longer-term enhancements are seen both in the power at wavebands

unabsorbed by hydrocarbons as well as that of an absorbed one in many cases (Tao et al., submitted to the same issue, hereafter referred to as Paper 1).

[6] In this study, we estimate the auroral electron energy and flux using the FUV CR method and explore further the magnetospheric plasma parameters using the Hisaki/EXCEED observations, in order to clarify the cause of auroral variations. HST/STIS (Space Telescope Imaging Spectrograph) spatially-resolved images are also utilised to derive a reference auroral area in the estimation procedure. EXCEED covers a different spectral range to STIS, so we define a CR for the EXCEED spectral analysis and obtain a CR-energy relation which is consistent with the previous CR for HST [Gérard et al., 2014]. The datasets and auroral parameter estimations are described in Sections 2 and 3, respectively. Section 4 describes the time variation of the derived auroral parameters and relationships between these parameters. Section 5 discusses the effects of assumptions used in the auroral parameter estimation, the derived current-voltage relation, and the possible explanations for these variations. Conclusions of this study are outlined in Section 6.

2. Datasets

[7] The datasets are the same as those used in Paper 1. Here we summarise important aspects related to the observations.

[8] EXCEED counts EUV photons as a function of spatial slit position and wavelength dispersion. A dataset was taken by using the dumbbell-shaped slit which detects emissions from the Io plasma torus and Jupiter's northern polar region simultaneously. The slit width at

the polar region is 20 arcsec in the north-south direction (along Jupiter's rotation axis) with the effective spatial resolution along the slit (dawn-dusk direction) of 17 arcsec [Yoshikawa et al., 2014] and a pointing accuracy of ± 2 arcsec. The auroral signal in slit cells covering 20 arcsec at specific wavelength ranges (described in Section 3) is integrated to yield the total emission from the northern polar region in this analysis. The red solid lines in Figure 1a shows the coverage of EXCEED auroral aperture in the north hemisphere. EXCEED detects auroral emission over 80–148 nm wavelength range, covering part of the H₂ Lyman (B \rightarrow X) and Werner (C \rightarrow X) band emissions with a resolution of 0.3 nm full width at half maximum (FWHM). Figure 1b shows an example spectrum taken on 2 January 2014. Here we analyze data from 21 December 2013 to 31 January 2014 when the EXCEED time coverage was maximum.

[9] The HST observations (ID: GO13035) acquired FUV images and spectra of Jupiter's northern aurora using the FUV-MAMA detector of STIS. Auroral images were taken using the SrF₂ long-pass filter to detect H₂ emission in the 125–170 nm wavelength range with 0.08 arcsec resolution. The 52 arcsec long \times 0.5 arcsec wide slit with the G140L grating provides imaging spectra over 110–170 nm with ~ 1.2 nm resolution. On each HST orbit, observations were made in the following sequence, image (700 sec), spectra (200 sec), and image (736 sec), using time-tag mode. We use time-integrated spectrum and images over each interval in this analysis. This sequence was repeated during 14 HST orbits spaced over two weeks. The observation date, time, and central meridional longitude (CML) are summarized in Table 1 of Paper 1. Figure 1a shows the HST image and slit position (white vertical line) for the spectrum

obtained on the same HST orbit shown by the black line of Figure 1b. Except for the geo-coronal emission range (e.g., around 121.6 nm Lyman- α) and the spectral edges, the spectra observed by EXCEED and STIS match well, although their apertures, covering the whole northern polar region for EXCEED and integration over the slit for STIS, are different.

[10] The lack of a solar wind monitor near Jupiter during the Hisaki observations is compensated by employing a one-dimensional (1D) magnetohydrodynamic (MHD) model which propagates the observed solar wind conditions around Earth to Jupiter [Tao et al., 2005]. We use OMNI 1-hour data as the input solar wind data. During the observations from 21 December 2013 to January 2014 of interest here, Jupiter was located at opposition on 6 January and the Earth-Sun-Jupiter angle was small enough ($< 50^\circ$) to estimate the arrival time of solar wind pressure enhancements with good, ~ 1 day accuracy.

3. Parameter Estimations

3.1 Color Ratio

[11] We use the typical FUV CR for STIS spectra defined as

$$\text{CR}_{\text{STIS}} = I_{(155-162 \text{ nm})} / I_{(123-130 \text{ nm})} \quad , \quad (1)$$

where I is the height-integrated intensity of the emission, in units of either kR or photons/sec.

We use the relation between electron energy and CR_{STIS} proposed by Gérard et al. [2014] (called the “atmosphere model 2” case there) to estimate the electron energy, which is shown by the black line in Figure 1c. This relation is obtained based on mono-energetic auroral

electron precipitation into a model atmosphere using a Monte Carlo method, including the cross sections extended up to relativistic electron energies. The derived electron energy– CR_{EXCEED} relation is specific to the choice of auroral electron distribution, atmospheric model, and methane altitude distribution. For example, a Maxwellian precipitating electron distribution could modify the estimated mean energy to be 50 keV instead of 79 keV for a monoenergetic population for $CR = 1.5$ [Gérard et al., 2014]. The dependence of the relation on this choice is described using other relations in Section 5.1.

[12] EXCEED covers the wavelength range up to 148 nm and thus CR_{STIS} is not directly applicable. An alternative CR_{EXCEED} is newly defined as

$$CR_{EXCEED} = I_{(138.5-144.8 \text{ nm})} / I_{(126.3-130 \text{ nm})} .$$

(2)

We select these two wavelength ranges for CR_{EXCEED} using the following criteria: (i) the absorption cross section of dominant absorber CH_4 is different enough in the two wavelength ranges (specifically, the ratio of the CH_4 absorption cross section averaged over 126.3–130 nm wavelength to that averaged over 138.5–144.8 nm is ~19), (ii) H_2 self-absorption is not effective at these wavelengths, i.e., >120 nm [e.g., Gustin et al., 2013], and (iii) EXCEED has good sensitivity with an effective area more than ~0.7 cm² (Figure 11 of Yoshikawa et al. [2014]).

[13] The relation between CR_{EXCEED} and auroral electron energy is derived consistently with the CR_{STIS} method by referring to the absorption cross section of methane (blue line in Figure

1b), as previously proposed by Gustin et al. [2002]. The observed spectral intensity including absorption by dominant absorber CH₄ can be expressed in terms of the absorption cross section σ of CH₄, the CH₄ column density N_{CH_4} , and the unabsorbed height-integrated spectrum intensity I' as

$$I_{(138.5-144.8 \text{ nm})} = I'_{(138.5-144.8 \text{ nm})} \exp(-N_{\text{CH}_4} \sigma_{(138.5-144.8 \text{ nm})}). \quad (3)$$

Using this and similar relations for other wavelength cases, we obtain expressions for the color ratio as

$$\begin{aligned} \text{CR}_{\text{STIS}} &= I_{(155-162 \text{ nm})} / I_{(123-130 \text{ nm})} \\ &= I'_{(155-162 \text{ nm})} / I'_{(123-130 \text{ nm})} \exp\{-N_{\text{CH}_4} (\sigma_{(155-162 \text{ nm})} - \sigma_{(123-130 \text{ nm})})\}, \quad (4) \end{aligned}$$

$$\begin{aligned} \text{CR}_{\text{EXCEED}} &= I_{(138.5-144.8 \text{ nm})} / I_{(126.3-130 \text{ nm})} \\ &= I'_{(138.5-144.8 \text{ nm})} / I'_{(126.3-130 \text{ nm})} \exp\{-N_{\text{CH}_4} (\sigma_{(138.5-144.8 \text{ nm})} - \sigma_{(126.3-130 \text{ nm})})\}. \quad (5) \end{aligned}$$

Substituting N_{CH_4} obtained from equation (4) into equation (5),

$$\text{CR}_{\text{EXCEED}} = I'_{(138.5-144.8 \text{ nm})} / I'_{(126.3-130 \text{ nm})} \times \{\text{CR}_{\text{STIS}} I'_{(123-130 \text{ nm})} / I'_{(155-162 \text{ nm})}\}^{\beta} \quad (6a)$$

$$\beta \equiv (\sigma_{(138.5-144.8 \text{ nm})} - \sigma_{(126.3-130 \text{ nm})}) / (\sigma_{(155-162 \text{ nm})} - \sigma_{(123-130 \text{ nm})}), \quad (6b)$$

where $I'_{(155-162\text{ nm})} / I'_{(123-130\text{ nm})} = 1.1$ [e.g., Gérard et al., 2014], $I'_{(138.5-144.8\text{ nm})} / I'_{(126.3-130\text{ nm})} = 0.59$ (estimated using the STIS spectra), and $\sigma_{(126.3-130\text{ nm})} = 1.73 \times 10^{-17} \text{ cm}^2$, $\sigma_{(138.5-144.8\text{ nm})} = 5.70 \times 10^{-19} \text{ cm}^2$, $\sigma_{(123-130\text{ nm})} = 1.74 \times 10^{-17} \text{ cm}^2$, and $\sigma_{(155-162\text{ nm})} = 5.33 \times 10^{-24} \text{ cm}^2$ are derived from Parkinson et al. [2006]. This value of $\text{CR}_{\text{EXCEED}}$ can then be related to the electron energy through the corresponding value of CR_{STIS} , as shown by the red line in Figure 1c. Since these definitions involve intensity in units of counts or kR, a factor of $(144.8+138.5)/(130+126.3) = 1.10$ or $(155+162)/(130+123) = 1.25$, which is a transformation from a photon number flux to an energy flux referring to the averaged wavelength in each band, is multiplied to the ratio of intensities in power units for EXCEED and STIS cases, respectively.

3.2 Estimations of Total Power and Flux

[14] The auroral electron energy flux is estimated using the power at less absorbed wavelengths 138.5–144.8 nm for EXCEED analysis. The conversions factor from power measured in this band to total power over 70–180 nm is estimated according to a spectral model based on Tao et al. [2011]. This model additionally includes the B' and D states are added with all transition coefficients [Fantz and Wunderlich, 2006], assuming the ratio of production rate of states B:C:B':D = 1:0.9:0.16:0.15 based on Perry et al. [1999]. The total emission power over 138.5–144.8 nm for EXCEED is multiplied by 44.4 to convert into total power over 70–180 nm. According to the conversion rate of input electron energy to UV emission, ~10% [e.g., Waite et al., 1983], the parameter is again multiplied by 10 to obtain the total input electron energy associated with the precipitating electrons entering the atmosphere.

3.3 Estimation of Auroral Area

[15] Knowledge of the emitting auroral area is required to estimate the electron flux values. Hisaki/EXCEED data contains emission from the whole northern polar region facing Earth. The observed auroral region (and therefore power) vary with CML. As in Figure 4 of Paper 1, the CML dependence of the observed auroral power is well correlated with the length of the region in the northern ionosphere mapping to an L-value of 30 of the VIP4 magnetic field model with a ring current referring to Table 4 of Connerney et al. [1998]. Therefore, we use a strip in the ionosphere along the latitudes corresponding to $L=30$ as an indicator of the auroral area. This assumes that all auroral power comes from this strip.

[16] For simplicity, we evaluate the effective width of the strip from the total number of pixels in the HST/STIS images which provide the same emitted power as the EXCEED observations. Since the wavelength ranges and filters are different, the intensities observed by STIS and EXCEED are converted into the total emitted power over 70–180 nm. We use the conversion factor provided by Gustin et al. [2012] for STIS image data. They provide the coefficients to convert from counts per second detected by STIS with the SrF2 filter to total emission power over 70–180 nm as a function of CR_{STIS} . Using the CR_{STIS} value determined from the main auroral oval for each spectrum taken during the same HST orbit, a conversion coefficient is determined for each image. We calculate the integrated power from a single image with various integration ranges; for example, we integrate power in the pixels which contain the intensity larger than a certain limit called “minimum intensity”, e.g., 0.1 (0.02) count/sec, to find the integrated power, e.g., ~460 (2300) GW for the case shown in Figure 2a. This integrated power is obtained with various “minimum intensities” as shown in Figure 2a. This decreasing profile

shows two structures, above and below the bump at the count rate $\sim 0.03 \text{ count s}^{-1}$. The pixels with higher count rate correspond to the aurora, while the smaller is due to disk emission. The total power observed by EXCEED is also converted into power over 70–180 nm using that measured at 138.5–144.8 nm, as described in Section 3.2.

[17] Using the 70–180 nm power estimates, the comparison of the auroral power from an EXCEED observation close in time to an HST image with a similar CML thus provides a specific minimum power for each image. Then we add up the ‘auroral’ pixels exceeding this minimum power for 14×2 images (two images are taken for each orbit), as shown as a function of CML in Figure 2b. The number of ‘auroral’ pixels determined in this way varies over $(2\text{--}7) \times 10^4$ pixels. The uppermost two points were taken on day of year (DOY) 11, corresponding to the EXCEED short-term power enhancement. The solid line in Figure 2b shows the CML profile obtained from the main auroral latitudes corresponding to a dipole L-value of 30 in the VIP4 magnetic field model [Connerney et al. 1998], multiplied by the width of 1250 km and divided by the HST pixel area on Jupiter. The observations are well within $\pm 40\%$ variation from this line as shown by dotted and dot-dashed line. Figure 2c shows the variation of auroral ‘width’ for each HST image, determined by assuming all the auroral pixels presented in Figure 2b come from the main oval strip as described. The mean value of the width is ~ 1250 km and the standard deviation over 28 points is 256 km. The auroral latitude is simply represented by that of the main aurora, so other structures such as polar emission would increase the effective emitting area, in addition to modification by non-uniform main aurora. In this estimation, we do not subtract the background emission in HST/STIS images,

which leads to over-estimation of the minimum count and under-estimation of the auroral area.

Despite this simplified estimation, the derived value, 1250 km ($\sim 1^\circ$ latitude), is a nominal width of the main oval region, which is in agreement with HST imaging observations. We adopt this value for all EXCEED data analysis (except for Figures 7 and 8).

[18] Using the effective auroral width of 1250 km multiplied by the CML-dependent length of a L-value of 30 in the VIP4 magnetic field model visible to the observer, we convert the spatially integrated emission value into values per unit area. The ambiguity in the modeled auroral location in latitude would not affect the estimated area because the same previous auroral latitude profile (used above and in Figure 2c) is used in this part of the analysis. The effect of the simple assumption of constant emitting area is evaluated in Section 5.1.

3.4 Estimation of Parameters per Unit Area

[19] Once the mean electron energy and electron energy flux are derived, the number flux is obtained from the latter parameter divided by the former. This number flux is then multiplied by the elementary electronic charge to obtain the current density.

3.5 Acceleration Theories

[20] Following the previous investigation for Jupiter's aurora by Gustin et al. [2004, 2006], we compare the estimated auroral electron flux-energy relation (derived from observations) with auroral acceleration theories by comparing the estimated electron flux to the theoretical field-aligned current and the electron energy to the theoretical field-aligned potential drop.

Here we refer to the Knight relation [Knight, 1973] and two extended relations for Jupiter by Cowley [2006] and Ray et al. [2009] as described in the introduction.

[21] Under the approximation of infinite mirror ratio, the Knight relation provides the potential drop $\Phi_{//}$ along the field line required to reach the necessary current density $j_{//}$ outside of the ionosphere and the energy flux E_f as [Cowley and Bunce, 2001; Gustin et al., 2004]

$$\frac{j_{//}}{j_{//0}} = 1 + \frac{e\Phi_{//}}{k_B T_0}, \quad (7)$$

$$\frac{E_f}{E_{f0}} = \frac{1}{2} \left[1 + \left(\frac{j_{//}}{j_{//0}} \right)^2 \right] = 1 + \frac{e\Phi_{//}}{k_B T_0} + \frac{1}{2} \left(\frac{e\Phi_{//}}{k_B T_0} \right)^2, \quad (8)$$

where $j_{//0}$ and E_{f0} are the current density and energy flux carried by precipitating magnetospheric electrons without acceleration, respectively, and k_B is the Boltzmann constant.

These can be expressed in terms of the magnetospheric plasma density N_0 and the thermal energy, which is assumed to have an isotropic Maxwellian distribution with temperature T_0 , as

$$j_{//0} = eN_0 \left(\frac{k_B T_0}{2\pi m_e} \right)^{1/2}, \quad (9)$$

$$E_{f0} = 2N_0 k_B T_0 \left(\frac{k_B T_0}{2\pi m_e} \right)^{1/2}. \quad (10)$$

Figure 3 shows the relationship between the potential drop, auroral electron energy flux, and number flux (current density) estimated from the Knight relation (black lines) for several

magnetospheric source densities. Since the accelerated electron energy, >several tens of keV, is much larger than the thermal energy of the source magnetospheric plasma $k_B T_0 \sim 2.5$ keV, we simply compare $\Phi_{//}$ with the accelerated electron energy inferred from the color ratio analysis.

[22] One extended model provides the relation including relativistic effects [Cowley, 2006]. Here we refer to one approximation which provides the largest deviation from the original relations (Eqs. (7) and (8)) under the limit $B/B_0 \rightarrow \infty$, where B_0 and B are respectively the magnetic field strength before and after passing the acceleration regions, represented as

$$\frac{j_{//}}{j_{//0}} = 1 + \frac{e\Phi_{//}}{k_B T_0} + \frac{1}{2} \frac{\left(\frac{e\Phi_{//}}{k_B T_0}\right)^2}{\frac{m_e c^2}{k_B T_0} + 1},$$

(11)

$$\frac{E_f}{E_{f0}} = 1 + \frac{e\Phi_{//}}{k_B T_0} + \frac{1}{2} \left(\frac{e\Phi_{//}}{k_B T_0}\right)^2 + \frac{1}{2} \frac{\left(\frac{e\Phi_{//}}{k_B T_0}\right)^3}{\frac{m_e c^2}{k_B T_0} + 3},$$

(12)

where c is the light velocity, and the source distribution $j_{//0}$ and E_{f0} are well represented by the non-relativistic formulae of Eqs. (9) and (10). The relationships between the derived parameters from this theory, using the same magnetospheric source parameters, are shown by the red lines in Figure 3.

[23] The other additional model is the current choke analytical form derived by Ray et al. [2009] based on a kinetic Vlasov model represented as

$$\frac{j_{//}}{j_{//1}} = 1 + (R_1 - 1) \left[1 - \exp\left(-\frac{e\Phi_{//}}{k_B T_1 (R_1 - 1)}\right) \right],$$

(13)

where $R_1 = 16$ (in this study), $j_{//1}$, and $k_B T_1$ are the magnetic mirror ratio, current density, and electron distribution temperature defined at the top of acceleration region, and $j_{//1}$ is provided by the same formula as Eq. (9) except we substitute N_1 and T_1 in place of N_0 and T_0 , respectively. The relationships between parameters according to this theory using the same plasma source parameters, for simplicity, are shown by the blue lines in Figure 3. The energy flux is estimated by the potential drop multiplied by the current density. Using this relation, the current density (hence energy flux) saturates for increasing potential drop.

4. Results

4.1 Derived Auroral Electron Parameters

[24] Figure 4 shows time variations of the auroral power observed by EXCEED and estimated parameters from 21 December 2013 (this date corresponds to day of year (DOY) -10 of the year 2014, where DOY 1 is 1 January 2014 and DOY 0 is 31 December 2013) to 31 January 2014 (DOY 31). The auroral powers shown and those used to determine CR_{EXCEED} in this paper have had subtracted from them a 5-day running average of those for which $0^\circ < CML < 30^\circ$ in order to exclude the solar backscatter from Jupiter's surface. These CML values in the range 0° – 30° correspond to the orientations for which the northern oval is least visible. We use data integrated over 10 minutes. The power emitted at wavelengths 138.5–144.8 nm (Figure 4a) and 126.3–130 nm (Figure 4b) show variations over several time scales, as reported in Paper 1. One

is the 10-hour planetary rotation period. In addition, there are two different types of enhancement: one is short-term, occurring within one rotation, on DOY 4, 11, and 14 [Kimura et al., 2015]. The other one is long-term (several rotations) at DOY -10– -6, DOY 1–2, and DOY 17–27. Short- (enhancement within one rotation) and long-term (more than one rotation) variations are shown by the orange and light-blue colors, respectively, excluding the intermittent observation during DOY-10–7 shown by the blue color. Neither the CR_{EXCEED} (Figure 4c) nor the estimated electron energy (Figure 4d) show a clear trend with these power variations, while there are more obvious enhancements in the electron flux (Figure 4f). For example, the electron energy during the short-term power enhancement on DOY 14 remains ~ 160 keV, which is comparable to or rather smaller than the values of 130–240 keV before or after the event, while the total electron number flux (Figure 4f) of $>10^{27} \text{ s}^{-1}$ or flux density (Figure 4g) of $>5 \times 10^{12} \text{ m}^{-2} \text{ s}^{-1}$ is larger than those, $< \sim 4 \times 10^{26} \text{ s}^{-1}$ or $2 \times 10^{12} \text{ m}^{-2} \text{ s}^{-1}$, before or after the event. For the long-term variations, flux enhancements are clearly seen until DOY -5, DOY 1–2, DOY 17–20, and DOY 21–27, while small energy enhancements are also seen in the DOY 1–2 and DOY 17–20 events. Comparing with the solar wind dynamic pressure at Jupiter estimated using a model (Figure 4i), these long-term variations show a good correspondence with dynamic pressure variations.

4.2 Electron Parameter Relationships

[25] The relationships between the electron energy flux, energy, and number flux (or current density) of the observed values are shown by the diamonds in Figure 5. The electron energy increases with energy flux in the range 0–50 mW m^{-2} , and then the energy remains < 200 keV

for 100–200 mW m⁻² range (Figure 5a). The current density or number flux increases with energy flux almost linearly (Figure 5b). The energy and current density relation (Figure 5c) appears to be made up of three components: electrons with energy 100–200 keV for large current density >0.4 μA m⁻², high energy electrons >250 keV for small current density ~0.2 μA m⁻², and a less clear correlation for the smaller current density and energy case. Following Gustin et al. [2004], who compared HST observations of Jupiter’s main aurora with the Knight acceleration theory, we add lines showing the relationships for the same parameters as they considered, i.e., magnetospheric plasma temperature $k_B T_0 = 2.5$ keV and density $N_0 = 0.0026$ cm⁻³ (solid line), 0.001 cm⁻³ (dashed), and 0.01 cm⁻³ (dot-dashed). It seems these upper and lower density cases restrict the observed parameters well. The points during the short- and long-term variations seen in Figure 4 are again shown by the orange and light-blue colors, respectively. Compared to other periods, both types of event correspond to electron energy of 100–200 keV with large energy flux >50 mW m⁻² and large current density >0.4 μA m⁻² parts, as seen in Figures 4d–4f.

[26] Although the obtained parameters represent the auroral emission integrated over the whole northern polar region, EXCEED has good time coverage. Next we show the time variation of these relations focusing on the short- and long-term power variations as seen in Figure 5. Figure 6a shows the time variation of emitted power at wavelength of 138.5–144.8 nm for the event observed on DOY14. Each event is categorized into several time steps: before the power enhancement (blue), during the power enhancement (red and orange) and power

decreasing phases or after enhancements (yellow, green, and light-blue). Two short-term and two long-term events are shown in Figures 6a–6d and Figures 6e–6h, respectively.

[27] Before the DOY 14 (Figure 6b) short-term event, the auroral electron energy and energy fluxes are distributed around the solid line taken from Gustin et al. [2004]. When the auroral power increases, the parameters reach ~ 150 keV and >130 mW m⁻² (red and orange), followed by the similar energy with lower energy flux (light green). Then the parameters, shown by green points, are recovered to the similar value with those before the event. The event on DOY 11 (Figure 6c) shows a less clear but similar variation. The initial enhancement achieves a relationship close to the Knight relation shown by the solid line, and then the energy flux increases to approach the relation shown by the dot-dashed line. Even after the event, the energy flux remains a bit larger than the previous values. A similar trend continues in the long-term variation events. Although the trend is less clear in the DOY -7 to -5 case (Figure 6f), the DOY 17–20 event (Figure 6h) shows auroral parameters initially lying almost between the solid and dashed-line, then an increase in energy flux to approach the dot-dashed line, followed by a decrease in energy flux to occupy the region similar to that before the event (light-blue, after DOY20.5).

[28] As in Figures 5 and 6, auroral power variations can be associated with magnetospheric parameters in the framework of acceleration theories. Figure 4h shows time series of the derived magnetospheric source plasma current density derived from Eq. (7) for an electron temperature of 2.5 keV based on Voyager observation [Scudder et al., 1981; Barbosa et al., 1979], which varies as $j_{//0} \times (2.5/k_B T_0$ [keV]). Referring to the derived electron energy for $e\Phi_{//}$,

$e\Phi_{//} \sim 100 \text{ keV} \gg k_B T_0$ is applied in this estimation. Note that this current density is measured just above the ionosphere. This varies from $1\text{--}5 \text{ nA/m}^2$ during the low power intervals up to $\sim 15 \text{ nA/m}^2$ for the short- and long-term intensification events. The possible relationships between density and temperature are discussed later (Section 5.4).

5. Discussion

5.1 Effect of Assumptions on Parameter Estimations and Validation

[29] In this Section, we discuss the effect of various assumptions on our analysis — namely, the CR-energy relation and assumption of constant auroral area.

[30] The CR is the ratio of auroral intensities in wavebands with and without strong CH_4 absorption. Therefore variations of the CH_4 altitude profile would modulate the CR even if the auroral electron energy remained constant. In this study, we assume that the CR reflects the electron energy variation. If CH_4 is transferred to higher altitude during auroral activity [i.e., Perry et al., 1999], then the derived electron energy would be overestimated and thus the electron flux underestimated. In this case, the obtained relationships would show a decreasing electron energy and increasing number flux to approach the Knight relation for larger N_0 (approaching the dot-dashed line in Figure 5a) or a steeper current-energy flux relation (Figure 5b), as quantitatively shown in the following test.

[31] Figure 7 represents the dependence of the relationship between energy flux and energy on the CR-energy model. Different CH_4 profiles modify this CR-energy model. We check using two relations: one from Gérard et al. [2003] (G1), and the other from model 1 of Gérard et al.

[2014] (G2), which have different hydrocarbon and electron energy profiles (Maxwellian and mono-energetic, respectively). These relations are shown in Figure 7a with the original one, model 2 of Gérard et al. [2014], labeled as G3, which is the same as that shown in Figure 1c. CR_{EXCEED} is estimated from their corresponding CR_{STIS} by the same method as described in Section 3.1. G1 corresponds to the case in which CH_4 is transferred upward most efficiently, and this CH_4 upwelling effect is greater in G2 than G3. The relation between energy flux and energy is distributed at a lower-energy range <150 keV for G1 (Figure 7b) and <200 keV for G2 (Figure 7c) compared to <300 keV for G3 (Figures 5a or 7e).

[32] In order to estimate the flux per unit area, we assume an auroral emission area corresponding to the main auroral oval region, which varies relative to the observer, i.e., the Earth, with Jupiter's rotation. As described in the Section 3.3, comparison with the HST images shows the variation of the area up to $\pm 40\%$. The estimated relations between electron energy flux and energy for wider (1750 km) and narrower widths (750 km) are shown in Figures 7d and 7f, respectively. The absolute value of estimated flux (here energy flux) is modified, while the relationships remain.

[33] As reported by Kimura et al. [2015], some power enhancements seen in EXCEED are associated with variation of the auroral area, according to the HST images. Here we quantitatively check this variable effect on the derived relationships of auroral parameters. We assume the auroral width to be constant only while the northern aurora faces the Earth ($<$ one planetary rotation). This assumption would be reasonable according to the previous HST continuous observations (e.g., Figure 6 of Nichols et al. [2009]). Figures 8b–8d are updated

relationships obtained from replacing the constant width 1250 km by the auroral strip width of each HST image for the parameter estimation from EXCEED observations in the same auroral aperture (as in Section 3.3 and Figure 2c). The power enhanced events (red points) occupy larger energy flux and current density regions with more restricted mean energy of 100–160 keV compared to the other intervals (orange), as in the constant width analysis (Figure 5). Therefore, the variation of auroral parameter relations appears valid even if the auroral area (morphology) varies temporally from event to event.

5.2 H₂ Self-absorption Effect

[34] As discussed by Livengood and Moos [1990], these CR variations are caused either/both by (i) electron energy variation and (ii) atmospheric, especially hydrocarbon profile, variations. This ambiguity also exists in our analysis, as discussed above (Section 5.1). One possible way to distinguish these two effects is a comparison with the H₂ self-absorption effect [Gustin et al., 2009]. The H₂ column density above the emission, which is detectable from the H₂ self-absorption effect, reflects how deeply the auroral electrons penetrate into the atmosphere. Since H₂ is the dominant atmospheric component, this method is independent of its atmospheric profile. Gustin et al. [2009] constrained the H₂ column density and vibrational temperature from the H₂ self-absorption effect using the high-resolved (~ 0.2 Å) spectra but could not constrain them from low-resolution (~ 5.5 Å) spectra. We examined EXCEED spectra with ~ 3 Å resolution but found that this H₂ self-absorption method is not applicable to constrain the H₂ density, i.e., electron energy.

5.3 Current-Voltage Relation

[35] We consider three acceleration theories. The current-choke relation seems to fit better for the polar dominant case as in Paper 1, i.e., when a larger increase in electron energy with energy flux is observed (Figure 5b of Paper 1 and blue solid line of Figure 3a). On the other hand, the linear increase of current density with energy flux (Figure 5b) is different from any models considered here. The relativistic effect should not be ignored for large electron energy, \sim a few 100s keV, as suggested by Cowley [2006]. The estimated relation suggests that the kinetic energy flux increases as the cube of the minimum potential or energy (red line of Figure 3a), and number flux increases more with energy flux than in the non-relativistic case (red line of Figure 3b). This trend is close to the observed linear trend at 40–80 mW/m² during enhanced events detected by EXCEED (color points of Figure 5b).

5.4 Time Variation

[36] According to the auroral electron acceleration theory, auroral power enhancements are associated with increase of $j_{//0}$ ($2.5/k_B T_0$ [keV]), where $j_{//0}$ is the current density which magnetospheric electrons can convey without acceleration. Using the relation of Eq. (9), this scaled current density increases linearly with the magnetospheric plasma density and decreases with source electron temperature as $\propto N_0 T_0^{-1/2}$, as shown by a contour map showing this dependence on the density and temperature (Figure 9). At the auroral-enhanced events, the value $j_{//0}$ ($2.5/k_B T_0$ [keV]) increases from ~ 3 up to ~ 15 nA/m² on DOY 14 and 17 (Figure 4h). There are possible physical explanations for the density and temperature variations responsible for variation of the current density. We discuss now those variations associated with two possible models.

[37] One is an adiabatic change of source plasma under a compression and/or plasma injection ((i) in Figure 10). The adiabaticity, $PV^\gamma = \text{constant}$, where P is pressure, V is flux tube volume (i.e., volume per unit magnetic flux), and $\gamma = 5/3$, is taken into consideration as an additional constraint. Since the hot plasma mainly contributes to the plasma pressure, $P = N_0 k_B T_0$. Mass conservation provides $VN_0 = \text{constant}$, for simplicity. Using these relations, we obtain the relation, $N_0^{-2/3} T_0 = \text{constant}$. This constraint on N_0 and T_0 variations is shown by white dotted lines in Figure 9 for five arbitrary constant values. For example, if the initial condition is $j_{//0}$ ($2.5/k_B T_0$ [keV]) ~ 3 at $k_B T_0 \sim 1.3$ keV and $N_0 \sim 1.5 \times 10^3 \text{ m}^{-3}$, these parameters can take values along the white dotted line to be $j_{//0}$ ($2.5/k_B T_0$ [keV]) ~ 15 at $k_B T_0 \sim 7.5$ keV and $N_0 \sim 2 \times 10^4 \text{ m}^{-3}$ under this adiabatic variation. The increase of the density by a factor of ~ 13 corresponds to a volume variation of $\sim 1/13$. An isotropic magnetospheric compression, for simplicity, achieves a radial decrease in size with a ratio of $(1/13)^{1/3} \sim 0.4$. The power enhanced event on DOY 17 is associated with the increase of solar wind pressure from 0.01 to 0.4 nPa. An empirical model represents the magnetopause distance $r_{\text{mp}}(P_{\text{sw}}) [R_J] = 35.5 / P_{\text{sw}}^{0.22}$, as a function of the solar wind pressure P_{sw} in nPa, based on previous spacecraft observations [Huddleston et al., 1998; Cowley and Bunce, 2003]. Using this model, r_{mp} changes from 97.7 to 43.4 R_J in this event. The ratio, 0.44, is comparable with the magnetopause radius variation ratio estimated above from a simple isotropic compression model.

[38] The other explanation is the change of the relative contribution of different auroral emission components ((ii) in Figure 10). Theoretical studies of the coupled magnetosphere-ionosphere-thermosphere system suggest the increase of auroral power at the

open-closed field line boundary with increasing solar wind pressure [Cowley et al., 2007; Yates et al., 2014]. This region is magnetically conjugate to a different plasma source in the magnetosphere via the magnetic field line compared to the main auroral oval. If we refer to electron characteristics of $N_0 = 2 \times 10^3 \text{ m}^{-3}$ and $k_B T_0 = 2.5 \text{ keV}$ based on the lower end of the density range measured by Voyager [Scudder et al., 1981; Barnhart et al., 2009], $j_{//0} (2.5/k_B T_0 [\text{keV}])$ becomes 3. The electron characteristics at the outer magnetosphere close to the open-closed boundary are $N_0 = 4 \times 10^3 \text{ m}^{-3}$ and $k_B T_0 = 0.25 \text{ keV}$ based on Ulysses observation [Phillips et al., 1993], which provides $j_{//0} (2.5/k_B T_0 [\text{keV}]) \sim 15$. Note that these density values are the lower end of the observed range, $\sim 20\%$ of the typical value of those referred to by Cowley et al. [2007]. The plasma density estimated in this study might be somewhat smoothed because the evaluation uses spatial-integrated auroral observations. Despite this limitation, the estimated parameter variations from ~ 3 up to ~ 15 , under changes of the relevant contribution of auroral components, are consistent with observed values.

[39] Large enhancements of the auroral power associated with $j_{//0} (2.5/k_B T_0 [\text{keV}])$ increases are seen with both short- and long-term variations. For the short-term variation, low latitude expansion of the main aurora is detected by the simultaneous HST observation [Kimura et al., 2015]. This would likely be related with the former, inward injection-like process, as this possibility is discussed by Kimura et al. [2015].

[40] Finally we raise questions about theoretical and observation studies which are not covered in this discussion. For (i), variation of the magnetospheric plasma angular velocity is not considered here, which should also impose constraints on the magnetosphere-ionosphere

coupled current system and auroral intensity. For (ii), the increase of the total auroral power associated with an increase in the relative contribution from aurora at the open-closed boundary during the large compression (as observed for the DOY 17 event) is consistent with the model proposed by Cowley et al. [2007]. Their modeling investigation showed both increase and decrease of the total precipitation energy due to large and small enhancements of solar wind pressure, respectively. A statistical investigation to test this behavior using EXCEED observations is an avenue for future work, including detailed analysis using high spatial-resolution images, e.g., by HST and JUNO, to check these scenarios.

6. Conclusions

[41] Auroral energy and flux parameters are derived from the quasi-continuous spectral observation by Hisaki/EXCEED. In this estimation, we also refer to the spatially-resolved HST/STIS image taken simultaneously on January 2014. The main results from this analysis are summarized as follows:

[42] (1) The enhancements of auroral power over short- and long- duration, associated with and without solar wind dynamic pressure enhancements, respectively, are mainly due to variations in the electron number flux, rather than the electron energy.

[43] (2) The relationships between auroral electron parameters are within those predicted by the Knight relation and two extended models of auroral acceleration, for the probable ranges of magnetospheric parameters.

[44] (3) The distribution of the relationships between auroral electron parameters during the short- and long-term auroral intensifications are shifted from the other periods: the energy flux and current density increases and the mean electron energy is restricted to 100–200 keV. A difference between short- and long-term events has not been found so far except for the variation in time scale.

[45] (4) Applying the auroral electron acceleration theory, magnetospheric source plasma parameters are estimated. Enhancements of the auroral power are associated with increases of the current density contributed by the magnetospheric source plasma. If the magnetospheric plasma experiences adiabatic variation under a magnetospheric compression and/or plasma injection, both the density and temperature would increase. Another possibility is a change in the dominant contributor of auroral power, from the main aurora to the emission at the open-closed boundary. The estimated parameter variations are in the low density range of the observed magnetospheric plasma.

Acknowledgements

[46] We acknowledge working teams of Hisaki/EXCEED, WIND, ACE, and OMNI. This work is also based on observations made with the NASA/ESA Hubble Space Telescope (observation ID: GO13035), obtained at the Space Telescope Science Institute, which is operated by AURA, Inc. for NASA. The data of Hisaki spacecraft are in the Data Archives and Transmission System (DARTS) of JAXA. This research was supported by a grant-in-aid for

Scientific Research from the Japan Society for the Promotion of Science (JSPS). SVB was supported by a Royal Astronomical Society Research Fellowship.

References

- Badman, S. V., G. Branduardi-Raymont, M. Galand, S. Hess, N. Krupp, L. Lamy, H. Melin, and C. Tao (2014), Auroral processes at the giant planets: Energy deposition, emission mechanisms, morphology and spectra, *Space Sci. Rev.*, doi:10.1007/s11214-014-0042-x.
- Barbosa, D. D., D. A. Gurnett, W. S. Kurth, and F. L. Scarf (1979), Structure and properties of Jupiter's magnetoplasma disc, *Geophys. Res. Lett.*, 6(10), 785–788.
- Barnhart, B. L., W. S. Kurth, J. B. Groene, J. B. Faden, O. Santolik, and D. A. Gurnett (2009), Electron densities in Jupiter's outer magnetosphere determined from Voyager 1 and 2 plasma wave spectra, *J. Geophys. Res.*, 114, A05218, doi:10.1029/2009JA014069.
- Connerney, J. E. P., M. H. Acuña, N. F. Ness, and T. Satoh (1998), New models of Jupiter's magnetic field constrained by the Io flux tube footprint, *J. Geophys. Res.*, 103(A6), 11929–11939, doi:10.1029/97JA03726.
- Cowley, S. W. H. (2006), Current-voltage and kinetic energy flux relations for relativistic field-aligned acceleration of auroral electrons, *Ann. Geophys.*, 24, 325–338.
- Cowley, S. W. H., and E. J. Bunce (2001), Origin of the main auroral oval in Jupiter's coupled magnetosphere-ionosphere system, *Planet. Space Sci.*, 49, 1067–1088.
- Cowley, S. W. H., and E. J. Bunce (2003), Modulation of Jupiter's main auroral oval emissions by solar wind induced expansions and compressions of the magnetosphere, *Planet. Space Sci.*, 51, 57–79.

Cowley, S. W. H., J. D. Nichols, and D. J. Andrews (2007), Modulation of Jupiter's plasma flow, polar currents, and auroral precipitation by solar wind-induced compressions and expansions of the magnetosphere: A simple theoretical model, *Ann. Geophys.*, *25*, 1433–1463.

Fantz, U., and D. Wunderlich (2006), Franck-Condon factors, transition probabilities, and radiative lifetimes for hydrogen molecules and their isotopomers, *Atomic Data Nuclear Data Tables*, *92*, 853–973.

Gérard, J.-C., J. Gustin, D. Grodent, J. T. Clarke, and A. Grard (2003), Spectral observations of transient features in the FUV Jovian polar aurora, *J. Geophys. Res.*, *108*(A8), 1319, doi:10.1029/2003JA009901.

Gérard, J.-C., B. Bonfond, D. Grodent, A. Radioti, J. T. Clarke, G. R. Gladstone, J. H. Waite, D. Bisikalo, and V. I. Shematovich (2014), Mapping the electron energy in Jupiter's aurora: Hubble spectral observations, *J. Geophys. Res. Space Physics*, *119*, doi:10.1002/2014JA020514.

Grodent, D. (2014), A Brief Review of Ultraviolet Auroral Emissions on Giant Planets, *Space Sci Rev*, doi: 10.1007/s11214-014-0052-8.

Grodent, D., J.-C. Gérard, J. T. Clarke, G. R. Gladstone, and J. H. Waite Jr. (2004), A possible auroral signature of a magnetotail reconnection process on Jupiter, *J. Geophys. Res.*, *109*, A05201, doi:10.1029/2003JA010341.

Gustin, J., D. Grodent, J.-C. Gérard, and J. T. Clarke (2002), Spatially resolved far ultraviolet spectroscopy of the Jovian aurora, *Icarus*, *157*, 91–103.

- Gustin, J., J.-C. Gérard, D. Grodent, S. W. H. Cowley, J. T. Clarke, and A. Grard (2004), Energy-flux relationship in the FUV Jovian aurora deduced from HST-STIS spectral observations, *J. Geophys. Res.*, *109*, A10205, doi:10.1029/2003JA010365.
- Gustin, J., S. W. H. Cowley, J.-C. Gérard, G. R. Gladstone, D. Grodent, and J. T. Clarke (2006), Characteristics of Jovian morning bright FUV aurora from Hubble Space Telescope/Space Telescope Imaging Spectrograph imaging and spectral observations, *J. Geophys. Res.*, *111*, A09220, doi:10.1029/2006JA011730.
- Gustin, J., J.-C. Gérard, W. Pryor, P. D. Feldman, D. Grodent, and G. Holsclaw (2009), Characteristics of Saturn's polar atmosphere and auroral electrons derived from HST/STIS, FUSE and Cassini/UVIS spectra, *Icarus*, *200*, 176–187, doi:10.1016/j.icarus.2008.11.013.
- Gustin, J., B. Bonfond, D. Grodent, and J.-C. Gérard (2012), Conversion from HST ACS and STIS auroral counts into brightness, precipitated power, and radiated power for H₂ giant planets, *J. Geophys. Res.*, *117*, A07316, doi:10.1029/2012JA017607.
- Gustin, J., et al. (2013), Effects of methane on giant planet's UV emissions and implications for the auroral characteristics, *J. Mol. Spect.*, *291*, 108–117.
- Huddleston, D. E., C. T. Russell, M. G. Kivelson, K. K. Khurana, and L. Bennett (1998), The location of the Jovian bow shock and magnetopause: Galileo initial results, *Adv. Space Res.*, *21*, 11, 1463–1467.
- Kimura, T., et al. (2015), Transient internally driven aurora at Jupiter discovered by Hisaki and the Hubble Space Telescope, *Geophys. Res. Lett.*, *42*, doi:10.1002/2015GL063272.
- Knight, S. (1973), Parallel electric fields, *Planet. Space Sci.*, *21*, 741–750.

- Livengood, T. A., and H. W. Moos (1990), Jupiter's north and south polar aurorae with IUE data, *Geophys. Res. Lett.*, *17*(12), 2265–2268.
- Morooka, M., T. Mukai, and H. Fukunishi (2004), Current-voltage relationship in the auroral particle acceleration region, *Ann. Geophys.*, *22*, 3641–3655.
- Nichols, J. D., J. T. Clarke, J. C. Gérard, D. Grodent, and K. C. Hansen (2009), Variation of different components of Jupiter's auroral emission, *J. Geophys. Res.*, *114*, A06210, doi:10.1029/2009JA014051.
- Pallier, L., and R. Prangé (2004), Detection of the southern counterpart of the Jovian northern polar cusp: Shared properties, *Geophys. Res. Lett.*, *31*, L06701, doi:10.1029/2003GL018041.
- Parkinson, C. D., J. C. McConnell, L. Ben Jaffel, A. Y. -T. Lee, Y. L. Yung, and E. Griffioen (2006), Deuterium chemistry and airglow in the Jovian thermosphere, *Icarus*, *183*, 451–470.
- Perry, J. J., Y. H. Kim, J. L. Fox, and H. S. Porter (1999), Chemistry of the Jovian auroral ionosphere, *J. Geophys. Res.*, *104*(E7), 16541–16565, doi:10.1029/1999JE900022.
- Phillips, J. I., S. J. Bame, B. L. Barraclough, D. J. McComas, R. J. Forsyth, P. Canu, and P. J. Kellogg (1993), Ulysses plasma electron observations in the Jovian magnetosphere, *Planet. Space Sci.*, *41*, 11/12, 877–892.
- Ray, L. C., Y.-J. Su, R. E. Ergun, P. A. Delamere, and F. Bagenal (2009), Current-voltage relation of a centrifugally confined plasma, *J. Geophys. Res.*, *114*, A04214, doi:10.1029/2008JA013969.

Sakanoi, T., H. Fukunishi, and T. Mukai (1995), Relationship between field-aligned currents and inverted-V parallel potential drops observed at midaltitudes, *J. Geophys. Res.*, *100*(A10), 19343–19360, doi:10.1029/95JA01285.

Scudder, J. D., E. C. Sittler Jr., and H. S. Bridge (1981), A survey of the plasma electron environment of Jupiter: A view from Voyager, *J. Geophys. Res.*, *86*(A10), 8157–8179, doi:10.1029/JA086iA10p08157.

Shiokawa, K., H. Fukunishi, H. Yamagishi, H. Miyaoka, R. Fujii, and F. Tohyama (1990), Rocket observation of the magnetosphere-ionosphere coupling processes in quiet and active arcs, *J. Geophys. Res.*, *95*(A7), 10679–10686, doi:10.1029/JA095iA07p10679.

Tao, C., R. Kataoka, H. Fukunishi, Y. Takahashi, and T. Yokoyama (2005), Magnetic field variations in the Jovian magnetotail induced by solar wind dynamic pressure enhancements, *J. Geophys. Res.*, *110*, A11208, doi:10.1029/2004JA010959.

Tao, C., S. V. Badman, and M. Fujimoto (2011), UV and IR auroral emission model for the outer planets: Jupiter and Saturn comparison, *Icarus*, *213*, 581–592.

Tao, C., L. Lamy, and R. Prangé (2014), The brightness ratio of H Lyman- α /H₂ bands in FUV auroral emissions: A diagnosis for the energy of precipitating electrons and associated magnetospheric acceleration processes applied to Saturn, *Geophys. Res. Lett.*, *41*, doi:10.1002/2014GL061329.

Waite, J. H., Jr., T. E. Cravens, J. Kozyra, A. F. Nagy, S. K. Atreya, and R. H. Chen (1983), Electron precipitation and related aeronomy of the Jovian thermosphere and ionosphere, *J. Geophys. Res.*, *88*(A8), 6143–6163, doi:10.1029/JA088iA08p06143.

Waite J. H., Jr. et al. (2001), An auroral flare at Jupiter, *Nature*, 410, 787–789,
doi:10.1038/35071018.

Yamazaki, A. et al. (2014), Field-of-view guiding camera on the HISAKI (SPRINT-A)
satellite, *Space Sci. Rev.*, 184, 1–4, 259–274, DOI: 10.1007/s11214-014-0106-y.

Yates, J. N., N. Achilleos, and P. Guio (2014), Response of the Jovian thermosphere to a
transient ‘pulse’ in solar wind pressure, *Planet. Space Sci.*, 91, 27–44.

Yoshioka, K. et al. (2013), The extreme ultraviolet spectroscope for planetary science,
EXCEED, *Planet. Space Sci.*, 85, 250–260.

Yoshikawa, I. et al. (2014), Extreme ultraviolet radiation measurement for planetary
atmospheres/magnetospheres from the earth-orbiting spacecraft (Extreme Ultraviolet
Spectroscope for Exospheric Dynamics: EXCEED), *Space Sci. Rev.*, 184, 1–4, 237–258,
DOI:10.1007/s11214-014-0077-z.

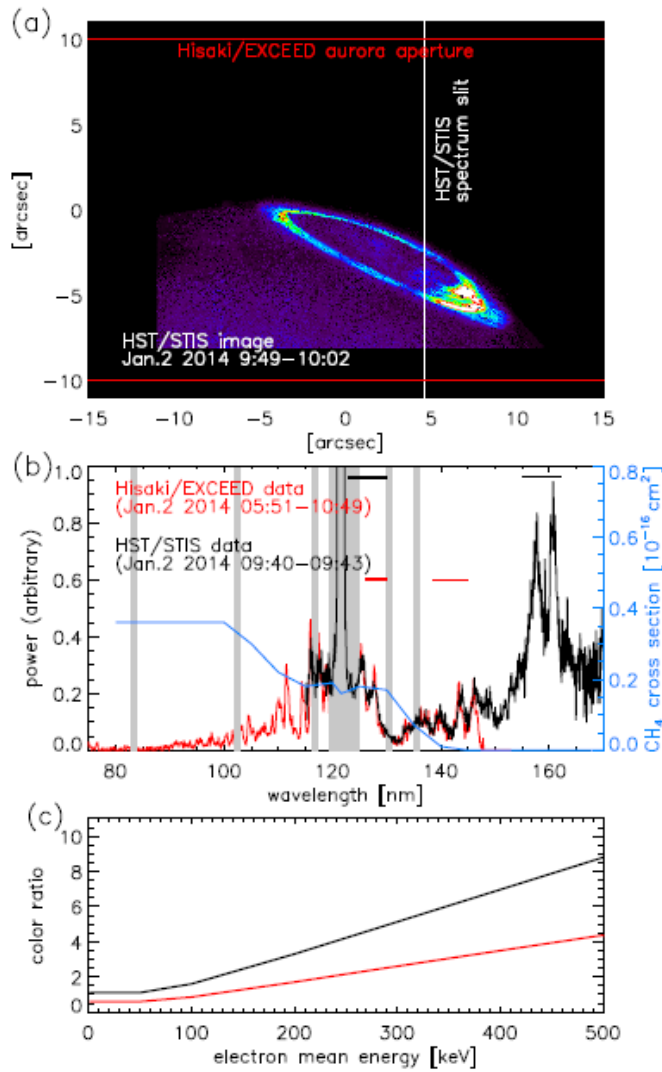


Figure 1. (a) HST/STIS image of Jupiter’s northern polar region, the position of the STIS slit (white vertical line) for spectrum observation on 2 January 2014, and Hisaki/EXCEED auroral aperture (area bounded by red lines), (b) auroral spectra taken by HST/STIS integrated over the slit (black) and Hisaki/EXCEED (red), and (c) relation between color ratio and mean energy of auroral electron. In Figure 1b, gray hatched regions correspond to the H Lyman and He emission lines from geocorona. Absorption cross section for the methane is overplotted by blue line referring to the right-hand axis. Red and black lines in Figure 1c are the color ratios for Hisaki/EXCEED (CR_{EXCEED}) and HST/STIS (CR_{STIS}), respectively, defined by intensity ratio of wavelengths shown by horizontal lines in Figure 1b.

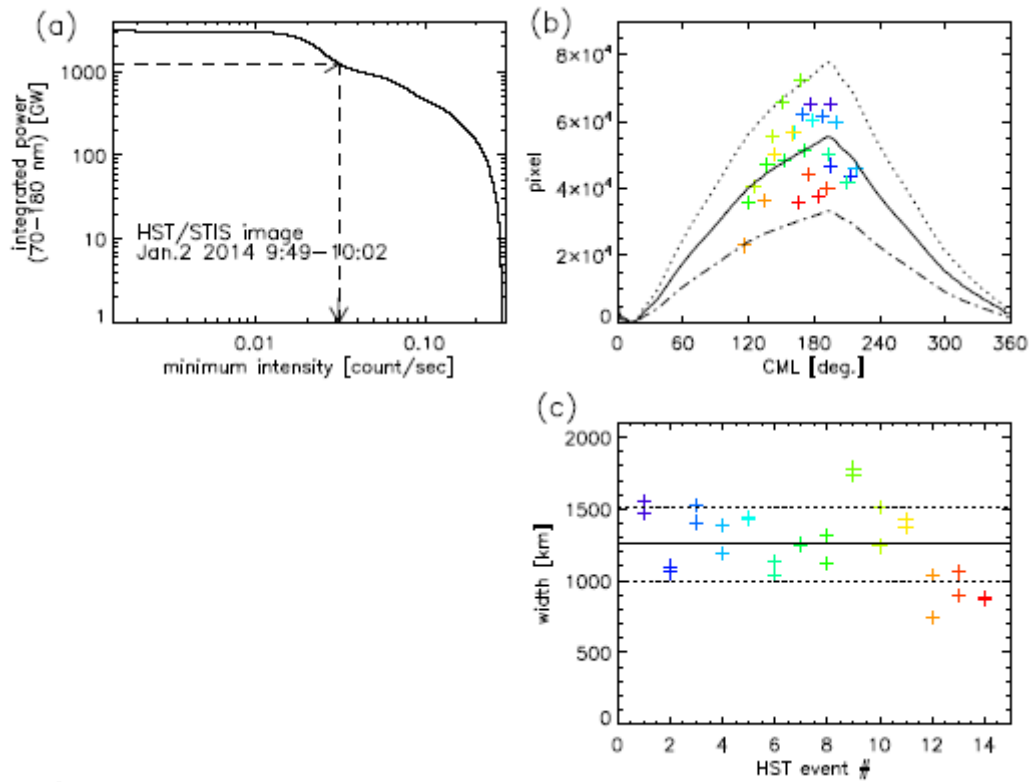


Figure 2. (a) Total intensity power of HST/STIS image taken on 2 January 2014, as a function of the integration minimum intensity. Intensity power from Hisaki/EXCEED close to this HST/STIS observation is shown by a horizontal dashed line to find the corresponding minimum intensity as a vertical dashed line. (b) Total ‘auroral’ pixels exceeding the minimum intensity as a function of CML, and (c) estimated width, for all 14×2 intervals. In Figure 2b, black solid line corresponds to the auroral area with 1250 km width, and dotted and dot-dashed lines are those added by +40% and -40%, respectively. Dotted and dot-dashed lines in Figure 2c are those added by $+\sigma$ and $-\sigma$, respectively, where σ is the variance of 256 km.

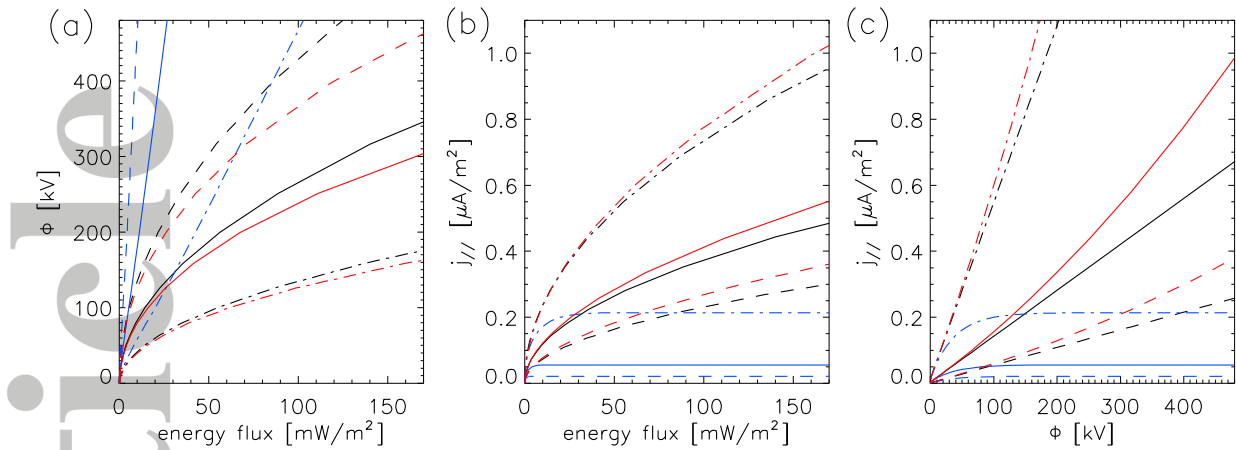


Figure 3. Relationships (a) between the potential drop and electron energy flux of precipitating auroral electrons, (b) between the current density and energy flux, and (c) between the potential drop and current density, estimated from acceleration theories. Black lines show those from the Knight relation with different source populations, $k_B T_0 = 2.5$ keV with $N_0 = 0.0026$ /cc (solid lines), $N_0 = 0.001$ /cc (dashed lines), and $N_0 = 0.01$ /cc (dot-dashed lines). Red lines are those including relativistic effect for $B/B_0 \rightarrow \infty$ case, and blue lines are from the current choke analytical form with the mirror ratio $R_1 = 16$ and $N_1 = N_0$ case.

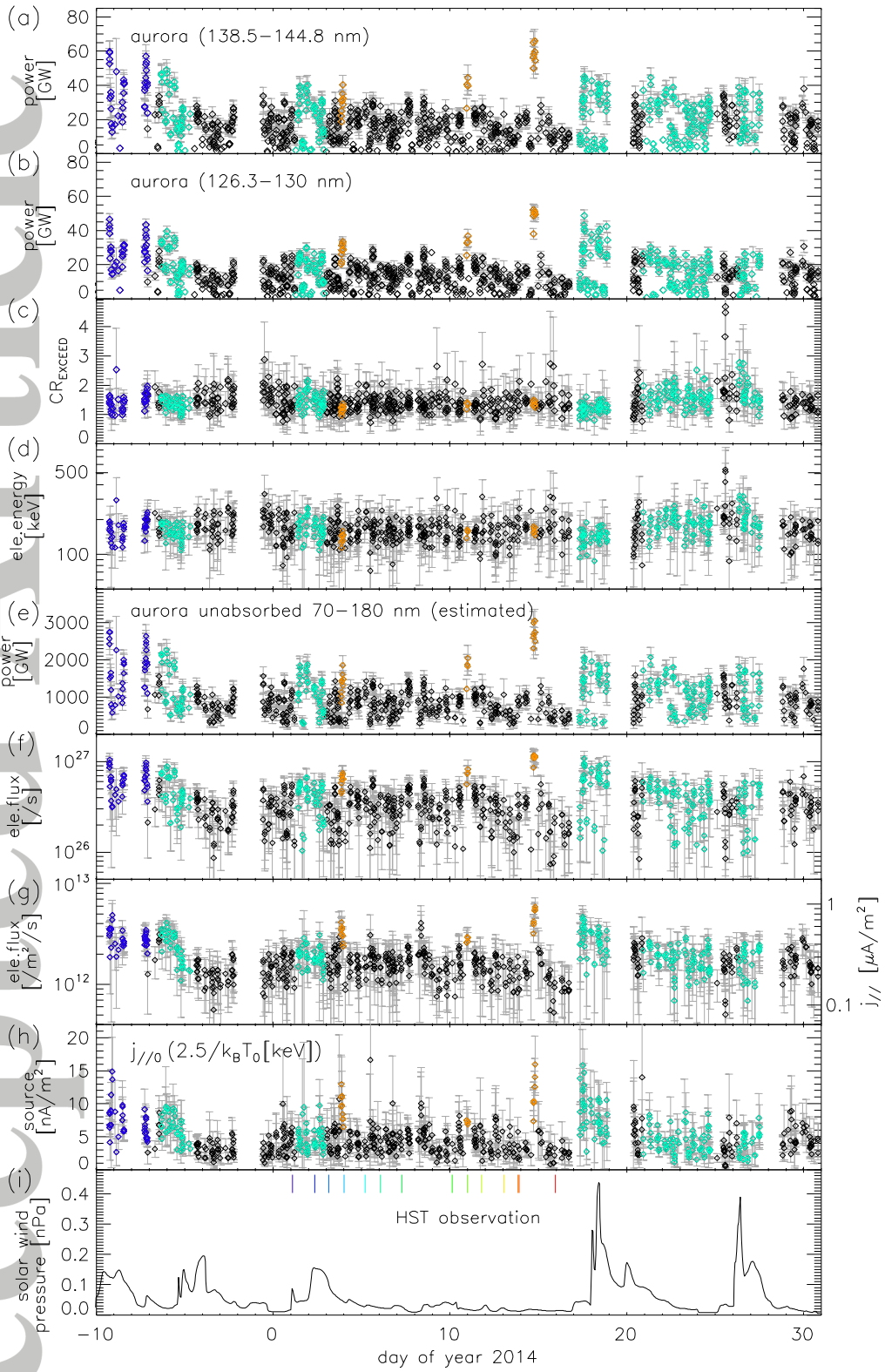


Figure 4. Time variations of (a) the power emitted at wavelengths 138.5–144.8 nm and (b) 126.3–130 nm, (c) the color ratio CR_{EXCEED} , (d) the auroral electron energy, (e) total unabsorbed H_2 power over wavelength 70–180 nm, (f) the auroral electron flux and (g) flux density, (h) the maximum field-aligned current that can be carried by precipitating magnetospheric electrons without field-aligned acceleration for electron temperature $k_B T_0 = 2.5$ keV case, and (i) solar wind dynamic pressure estimated from a 1D MHD model. Corresponding current density is shown in the right axis of Figure 4g. Short-term and long-term auroral power enhancements are shown in orange and light-blue colors, respectively, except for the intermittent observation before DOY-7 as shown in blue. Gray vertical lines of Figures 4a–4h show observational errors.

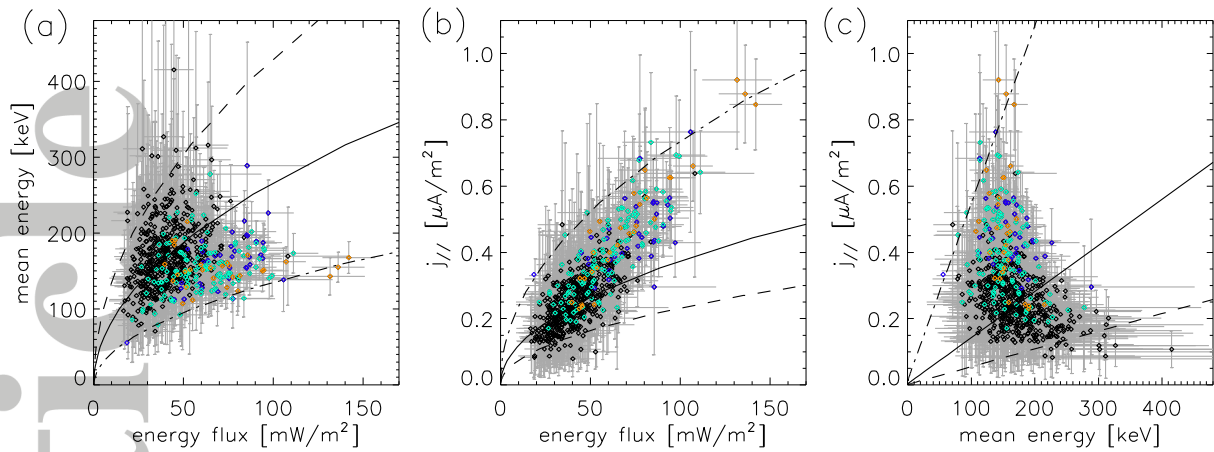


Figure 5. Relationships (a) between the mean energy and energy flux of the precipitating auroral electrons, (b) between the current density and electron energy flux, and (c) between the electron energy and current density, estimated from the 10-min-integrated Hisaki/EXCEED observations (black dots) with error bars (gray lines). The Knight relation are shown for different source populations, $N_0 = 0.0026$ /cc (solid lines), $N_0 = 0.001$ /cc (dashed lines), and $N_0 = 0.01$ /cc (dot-dashed lines). Orange and light-blue points are identical short-term and long-term auroral power enhancements, respectively, the intermittent observation before DOY-7 shown by blue, as in Figure 4.

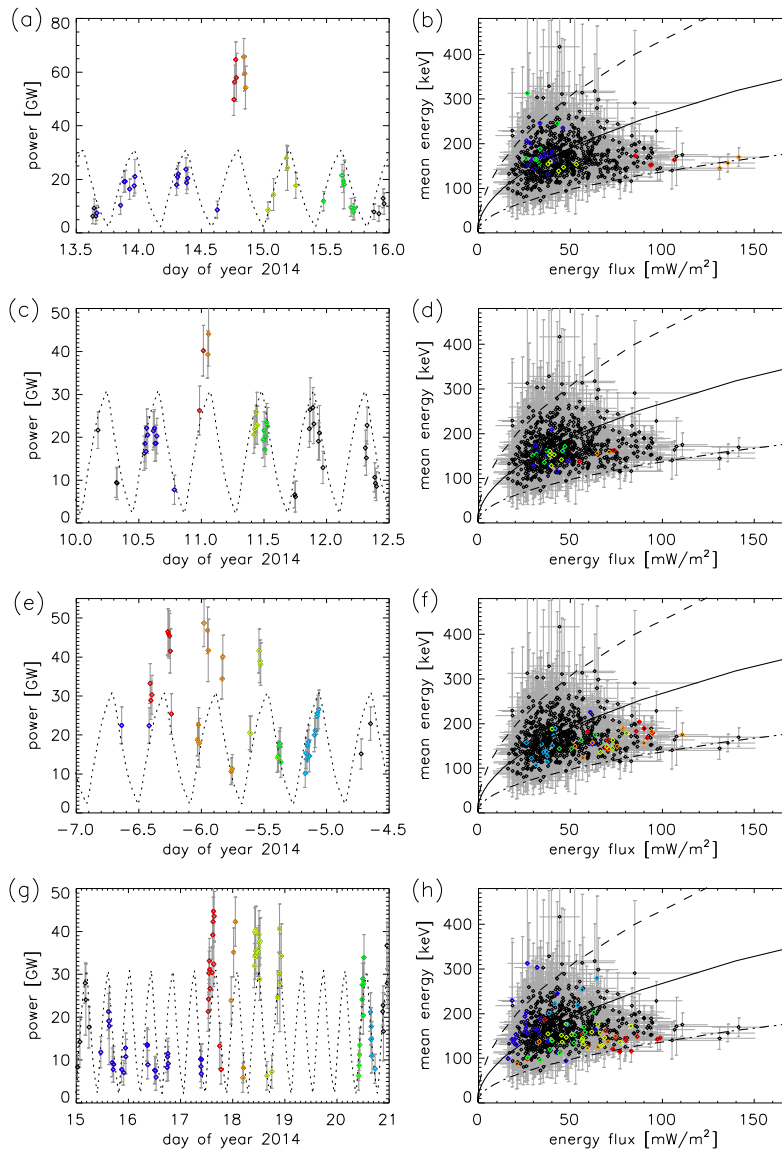


Figure 6. Time variation of auroral power emitted at wavelength 138.5–144.8 nm and temporal variation of the relation between the mean energy and energy flux of the precipitating auroral electrons around two short-term enhancements on (a)(b) DOY 14 and (c)(d) DOY 11, and two long-term enhancements on (e)(f) DOY -7–-5 and (g)(h) DOY 17–20, respectively. Dotted line in Figures 6a, 6c, 6e, and 6g are the scaled northern auroral area, as a function of CML at each time. Black dots in Figures 6b, 6d, 6f, and 6e are all points from observation from DOY -10 to 31, and color shows temporal variation corresponding with those colors in Figures 6a, 6c, 6e, and 6g, respectively.

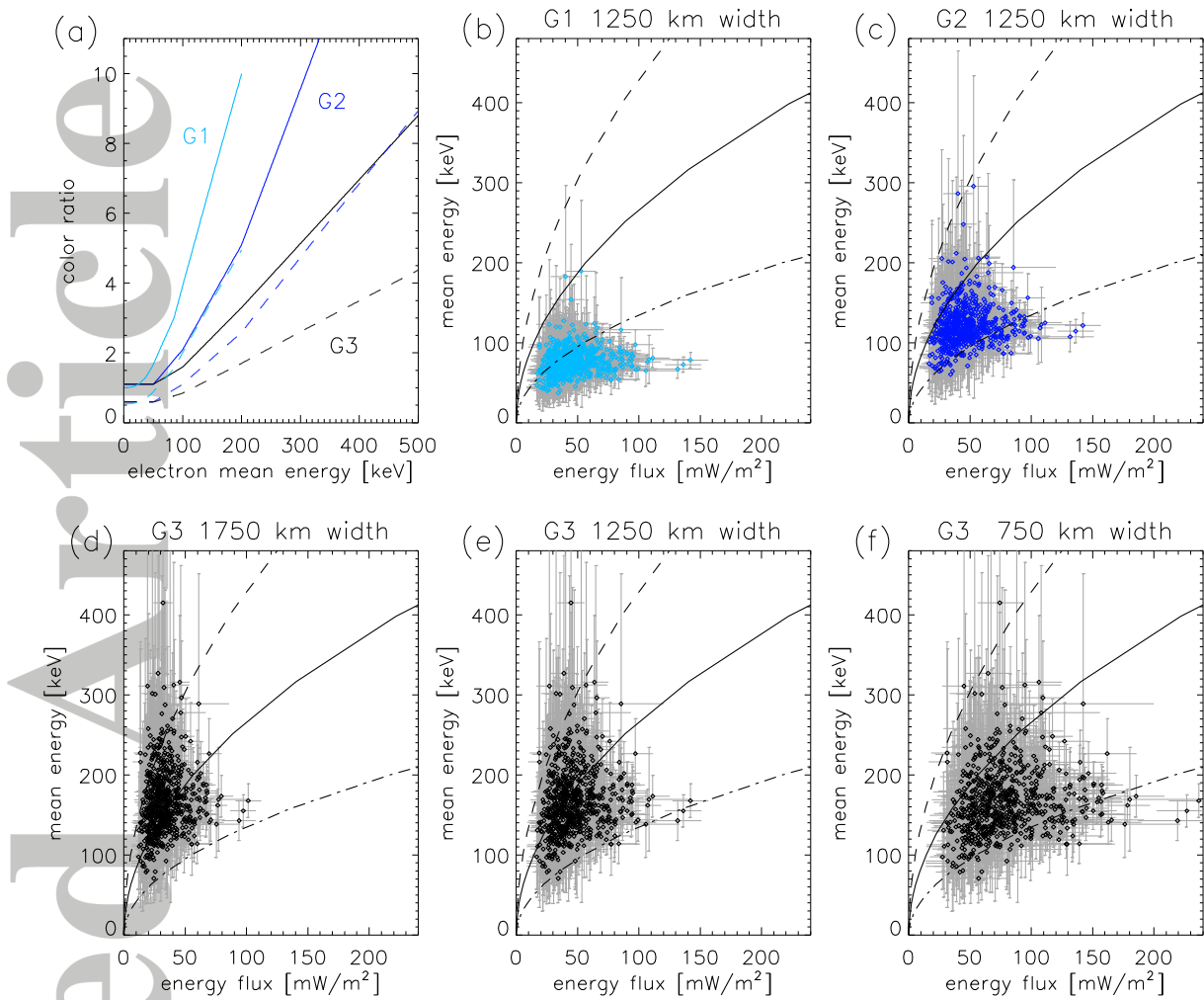


Figure 7. (a) Relationships between color ratio and mean energy of auroral electron under different model settings: Gérard et al. [2003] (light-blue, G1), atmosphere model 1 (blue, G2) and model 2 (black, G3) of Gérard et al. [2014] for CR_{STIS} (solid) and CR_{EXCEED} (dashed), and estimated relations between energy flux and energy using Hisaki/EXCEED data referring the color ratio-energy relations of (b) G1, (c) G2, and G3 with auroral width of (d) 1750 km, (e) 1250 km, and (f) 750 km. The plotting format is the same with that of Figure 5a except for colors corresponding to the energy-CR relations in Figure 7a.

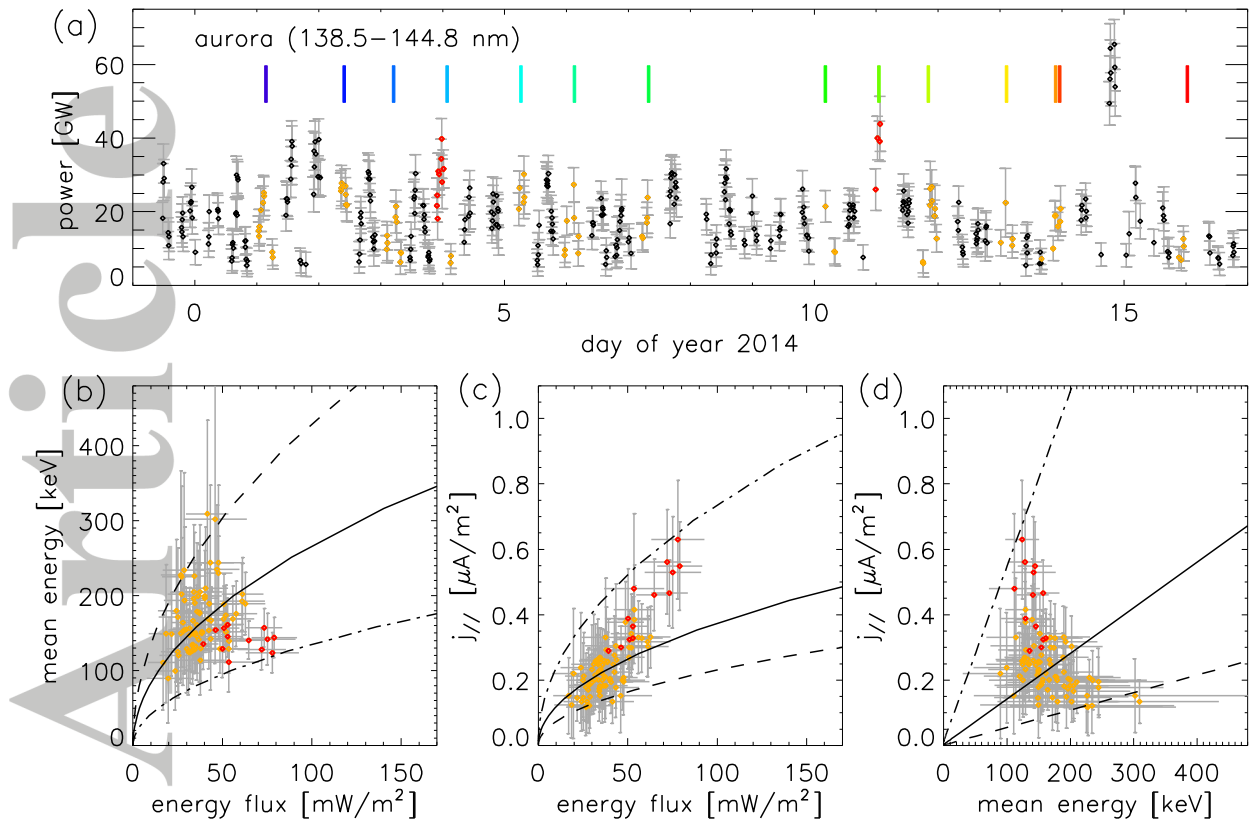


Figure 8. Time variations of (a) the power emitted at wavelengths 138.5–144.8 nm and relationships (b) between the mean energy and energy flux of the precipitating auroral electrons, (c) between the current density and electron energy flux, and (d) between the electron energy and current density, estimated from the 10-min-integrated Hisaki/EXCEED observations (points) with the error bars (gray lines). Observations during the Jupiter northern aurora facing observer just before and after the HST/STIS observations are shown by orange color. The power enhanced events among them are shown by red color. Vertical color lines in Figure 8a show the timing of HST observations.

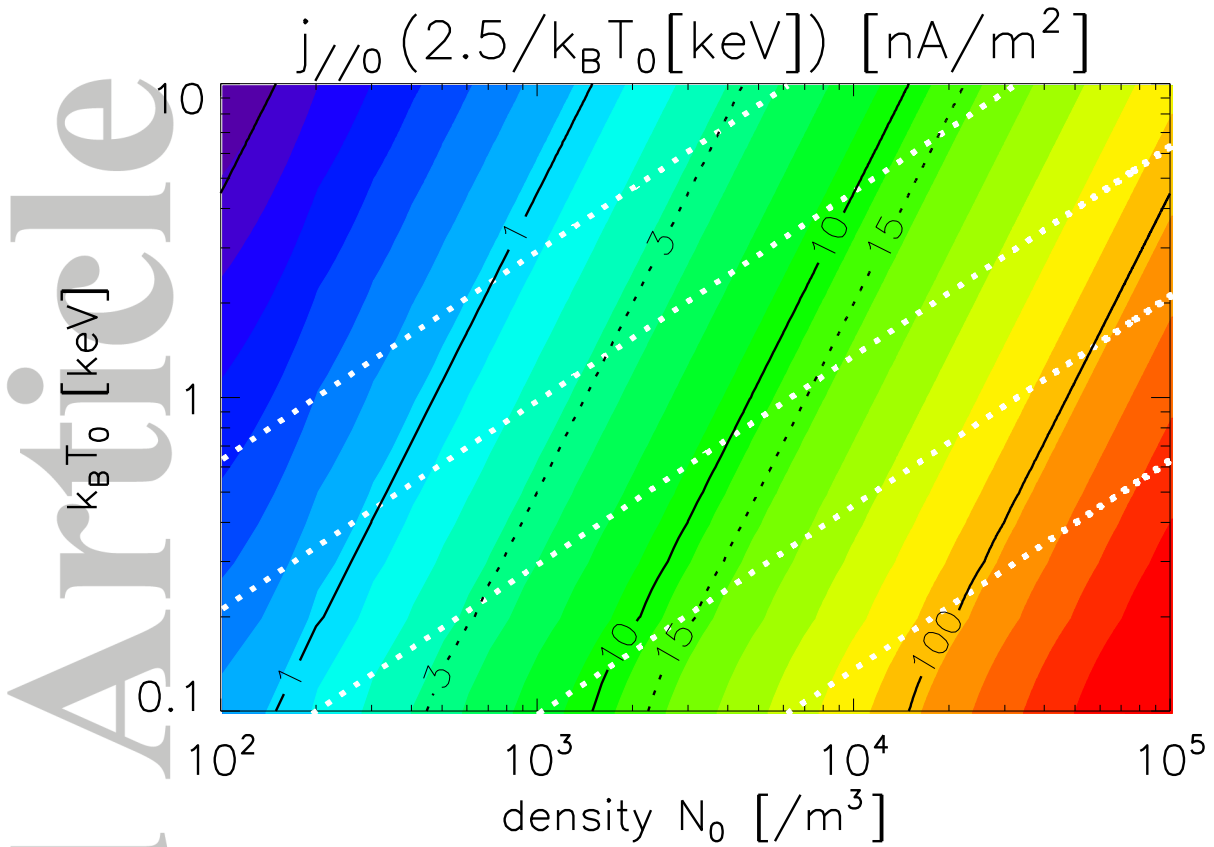


Figure 9. Contour (color and black lines) of the maximum field-aligned current that can be carried by precipitating magnetospheric electrons without field-aligned acceleration multiplied by $2.5/(k_B T_0 \text{ [keV]})$, as functions of number density and temperature at the magnetospheric equator. White dotted lines are variable trails of plasma under the adiabatic variation.

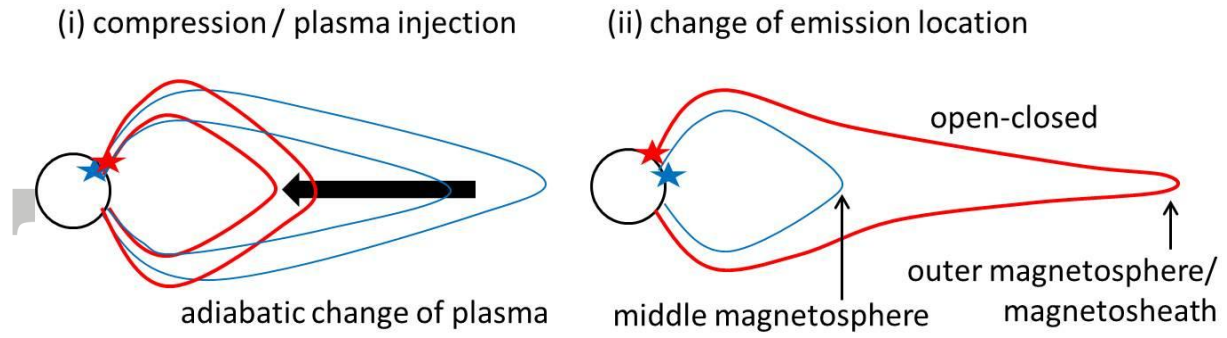


Figure 10. Possible explanations for the auroral power enhancement events (see the text for detail). Schematic of magnetic field lines before and during enhancements are shown by blue and red lines, respectively, and stars indicate the location of dominant aurora on the planet.

Accepted Article